SIMULATION, DESIGN, AND FABRICATION OF DEEP UV ALUMINUM GALLIUM NITRIDE DISTRIBUTED BRAGG REFLECTORS

A Thesis

Presented to the Faculty of the Graduate School

of Cornell University

in Partial Fulfillment of the Requirements for the Degree of

Master of Science in Materials Science & Engineering

by

Andrew Donald Devine

August 2018

ABSTRACT

The AlGaN materials system has been widely explored for its applications in wide-bandgap optoelectronics active in the UV-C spectrum between 300 - 200 nm. However, serious challenges to its use exist, including a lack of high reflectivity mirror components. Distributed Bragg Reflectors (DBRs) offer some of the most efficient mirrors available in this range. These one dimensional photonic crystals can be grown epitaxially on existing deep UV optical devices within the same growth chamber, making them easy to integrate with existing designs to potentially improve light extraction efficiency. Serious challenges still exist with the use of AlGaN DBRs, including the low contrast of the material system and difficulty of consistent crystal growth.

The design of AlGaN DBRs is approached from initial principles based on the optical simulation of these DBRs using the 1D transfer matrix method combined with existing models of the optical parameters of AlGaN films. Exotic approaches such as porous films are also included in the models to expand the range of design parameters. Design rules of thumb based on analysis of these simulations are used to simplify design choices into a systematic approach. Finally, the growth of AlGaN DBRs using molecular beam epitaxy (MBE) and optical and structural characterization methods are introduced.

BIOGRAPHICAL SKETCH

Andrew Devine is a Master of Science student in the Cornell Department of Materials Science and Engineering. He graduated from Cornell University with a B.S. in Materials Science and Engineering in 2017. His research interests include advanced semiconductor optical devices and photonic engineering, as well as their potential applications in quantum computing.

For Oma

ACKNOWLEDGEMENTS

I would like to make several acknowledgements for those who have helped me greatly in this work:

Professor Jena, for taking me on as a research student two years ago despite the last minute nature of the request,

Kevin Lee, for his invaluable technical expertise with Molecular Beam Epitaxy and assistance with the growth and characterization of DBR samples,

Shyam Bharadwaj, for his help with sample processing and learning how to get things done around here,

Professor Umbach, for helping spark my interest in the field of optoelectronics with a simple chat about metamaterials,

And most of all, my family, for the unceasing love and support they have given me since day one.

Thank you all.

-Andrew Devine

This work was supported by the NSF DMREF Program - NSF Grant DMREF-1534303

This work made use of the facilities of the Cornell Center for Materials Research - NSF Grant DMR-1719875

This work made use of the facilities of the Cornell Nanofabrication Facility - NSF Grant ECCS-1542081

TABLE OF CONTENTS

LIST OF TABLES

LIST OF FIGURES

CHAPTER 1

INTRODUCTION

1.1 Deep UV Optoelectronics in the AlGaN system

The discovery of the wide bandgap III-V semiconductor system based on gallium nitride (GaN), indium nitride (InN), and aluminum nitride (AlN) has allowed for major developments in visible light optoelectronics. The compound semiconductor system has a direct bandgap throughout the visible range and is consequently optically active throughout the entire range of possible bandgap energies. Until recently, feasible optoelectronic devices were confined to using photons with energies less than 3.4 eV (365 nm wavelength), the approximate band gap of GaN. This was due primarily to low conductivity in p-type AlGaN regions. However, the discovery of new methods of increasing the conductivity of p-type doped AlGaN [1],[2] has allowed this range to cover the entire UV-C spectrum. With these new techniques, devices using photon energies up to 6.2 eV (200 nm wavelength) are possible.

Devices such as LEDs in the UV-C range have already been demonstrated [3], although wall-plug efficiency in these devices is lower than 1 %. Deep UV laser diodes have proven elusive [4], due in large part to the difficulty of supplying enough carriers to the active region to achieve enough optical gain to reach the lasing threshold. Another major difficulty is the lack of suitable cavity mirrors. Typically, diode lasers use low-reflectivity facet mirrors created when the crystal is cleaved into individual diodes. This is a simple solution, but the low-reflectivity mirrors mean that most light escapes the cavity, and thus the lasing threshold of facet cavities is impractically high for wide bandgap semicon-

ductors like AlGaN. An alternative solution is to use a pair of high reflectivity mirrors to increase the Q-factor of the laser cavity, leading to a lower threshold necessary to begin lasing. This is the principle of the vertical cavity surface emitting laser (VCSEL), which uses Distributed Bragg Reflectors (DBRs) as mirrors.

1.2 Distributed Bragg Reflectors

The Distributed Bragg Reflector (DBR) may be considered the simplest type of photonic crystal. It is a one dimensional structure that creates a narrow and highly reflective stopband, in which nearly all light is reflected back along the optical axis. At its simplest level, a DBR is nothing more than a periodic stack of media with alternating high and low refractive indexes. Because of the relative simplicity of the structure, it can be easily incorporated into epitaxially-grown device designs. The DBR is one of the key optical components in a VCSEL, where a pair of very high reflectivity DBRs is used to create a laser cavity. Beyond VCSELs, DBRs also have potential applications in LEDs, where they can be used to increase light extraction efficiency [5].

1.3 AlGaN for Distributed Bragg Reflectors

While DBRs have been widely used in visible-light optoelectronics, they have not been as widely exploited in UV devices. This may be due to the lack of suitable wide-bandgap materials that can be epitaxially grown. AlGaN does not at first appear to be an ideal choice for a DBR, as the materials system does not offer the high refractive index contrast necessary to create a short and ef-

ficient Bragg reflector. However, AlGaN does offer a few critical advantages: It can be easily incorporated into existing growth processes for AlGaN-based optoelectronics, and it can be transparent up to photon energies of 6.2 eV (for pure AlN). These choices make it the primary candidate materials system for DBRs targeted within the deep UV spectrum. AlGaN has several features that make designing and growing DBRs complicated, such as a rapidly varying index of refraction, subthreshold absorption below the band gap edge, and difficulty with the growth of smooth surface morphologies for alloy fractions high in aluminum. Additionally, the demonstration of porous DBR structures has indicated the potential for greater reflective efficiency. These factors make it necessary for a complete model to be built to assist in the design and fabrication of DBRs in the deep UV range.

1.4 Thesis Structure

The purpose of this thesis is to create a semi-comprehensive guide to simulating, designing, and growing a distributed Bragg reflector using the AlGaN material system. As such, the thesis is divided into three main sections:

- Modeling Deep UV Distributed Bragg Reflectors - Explains the use of the transfer matrix method to model 1D optical systems and provides simple models for optical constants in the AlGaN system.
- Design Principles for Deep UV Distributed Bragg Reflectors - Explains the principles behind DBR design, including the calculation of center wavelength, stopband width, and peak reflectivity.

- Epitaxial Growth of Deep UV Distributed Bragg Reflectors and Characterization Methods - Briefly discusses the techniques used to grow an AlGaN DBR by Molecular Beam Epitaxy, as well as laboratory techniques used to characterize both the structure and optical properties of the grown samples.

CHAPTER 2

MODELING DEEP UV DISTRIBUTED BRAGG REFLECTORS

2.1 The Transfer Matrix Method for 1D Optical Systems

A distributed Bragg reflector is a periodic structure with many periods of high- and low-refractive index media. Simple calculations of reflectivity via the Fresnel equations (see equations (2.1) and (2.2)) become complicated due to the repeated Bragg reflections within the structure; Thus, a different method must be used to efficiently analyze the propagation of light within a DBR.

$$R_{TE} = |\frac{n_1 cos(\theta_i) - n_2 cos(\theta_t)}{n_1 cos(\theta_i) + n_2 cos(\theta_t)}|^2 \tag{2.1}$$

$$R_{TM} = |\frac{n_1 cos(\theta_t) - n_2 cos(\theta_i)}{n_1 cos(\theta_t) + n_2 cos(\theta_i)}|^2 \tag{2.2}$$

One of the most useful methods for analyzing light propagation in complicated structures is the one-dimensional transfer matrix method [6],[7]. This method can be used to replicate the results of more complicated coupled mode analysis with relatively simple computational steps. The transfer matrix method begins by defining the amplitudes A_f and A_b as the amplitudes of a forward moving wave and a backward moving wave, respectively. These amplitudes are related to a transfer matrix $\mathbf{T}_{12}$ by equation (2.3).

$$\begin{bmatrix} A_f^{n1} \\ A_b^{n1} \end{bmatrix} = \mathbf{T}_{12} \begin{bmatrix} A_f^{n2} \\ A_b^{n2} \end{bmatrix} \tag{2.3}$$

In short, the transfer matrix $\mathbf{T}_{12}$ couples the amplitudes of the forward and backward waves in the high-refractive index medium (n_1) with those in the low-refractive index medium (n_2). A similar matrix $\mathbf{T}_{21}$ exists for waves moving

from the low-refractive index medium to the high-refractive index medium. The problem can now be modeled as a simple one dimensional interface reflection at normal incidence. Thus, the form of the transfer matrix $\mathbf{T}_{12}$ can be simplified to:

$$\mathbf{T}_{12} = \begin{bmatrix} 1 & 1 \\ n & -n \end{bmatrix} \tag{2.4}$$

This is the decomposed form of the interface matrix, which will be useful in modeling complex structures, as it can be easily inserted into a periodic expression, as in eq.(2.14). It is important to note that the form of this matrix differs for TE and TM polarized light. At normal incidence, both match the form of equation (2.4). The full interface matrices are [8]:

$$\mathbf{T}_{12}^{TE} = \begin{bmatrix} 1 & 1 \\ ncos(\theta) & -ncos(\theta) \end{bmatrix} \tag{2.5}$$

$$\mathbf{T}_{12}^{TM} = \begin{bmatrix} cos(\theta) & cos(\theta) \\ n & -n \end{bmatrix} \tag{2.6}$$

Perhaps unsurprisingly, the opposite process $\mathbf{T}_{21}$ is simply the inverse of the $\mathbf{T}_{12}$ matrix:

$$\mathbf{T}_{21} = \begin{bmatrix} 1 & 1 \\ n & -n \end{bmatrix}^{-1} \tag{2.7}$$

It must be noted that these matrices must be *paired* to be meaningful, as the decomposition is used to seperate the ”halves” of the interface matrix. This means that two additional end matrices are required to complete multilayer analysis at the terminating points of the DBR structure. These matrices have identical forms to the matrices given in equations (2.4) and (2.7), with the exception of substituting in the necessary refractive indexes for the surrounding media.

The DBR also has lengths in which the forward and backward waves propagate in a medium with constant refractive index. These lengths are important,

as they determine the constructive interference conditions that create the optical stopband. Following the model of plane waves in a medium, we can describe the forward-propagating and backward-propagating waves as:

$$A_f(\mathbf{r}, t) = A_0 * e^{-i(k_n \cdot \mathbf{r} - \omega t)} \tag{2.8}$$

$$A_f(\mathbf{r}, t) = A_0 * e^{i(k_n \cdot \mathbf{r} - \omega t)} \tag{2.9}$$

To apply this to the transfer matrix method, time variance is removed, as only the standing waves inside the structure are of interest. The "propagating in medium" matrix $\mathbf{M}_t$ is then defined as:

$$\mathbf{M}_t \equiv \begin{bmatrix} e^{-i(k_n \cdot D)} & 0 \\ 0 & e^{i(k_n \cdot D)} \end{bmatrix} \tag{2.10}$$

Where D is the length of the medium along which the wave travels. In the simplest case of normal incidence, this is equivalent to the thickness of the layer. k_n is the wavevector in the medium, which is simply the free-space wavevector k_0 divided by the refractive index of the medium.

With these elements in place, the problem of propagation through the structure has been simplified in a series of steps. For example, the problem of entering a medium with refractive index n, passing through it, and exiting through a substrate (see Fig. 2.1) can now be simply described by the matrix equation (2.11).

$$\begin{bmatrix} A_f^{n1} \\ A_b^{n1} \end{bmatrix} = \mathbf{B}^{-1}\mathbf{T}_{12}\mathbf{M}_t\mathbf{T}_{21}\mathbf{B} \begin{bmatrix} A_f^{n2} \\ A_b^{n2} \end{bmatrix} \tag{2.11}$$

Where $\mathbf{B}$ are the end matrices previously discussed and $\mathbf{M}_t$ and $\mathbf{T}_{12}$,$\mathbf{T}_{12}$ are the matrices defined by eqs. (2.10), (2.4), and (2.7), respectively. Because the matrix $\mathbf{T}_{12}\mathbf{M}_t\mathbf{T}_{21}$ remains the same for the same material (regardless of what material surrounds it), it is convenient to define this as a "layer" matrix $\mathbf{L}_n$:

$$\mathbf{L}_n = \mathbf{T}_{12}\mathbf{M}_t\mathbf{T}_{21} \tag{2.12}$$

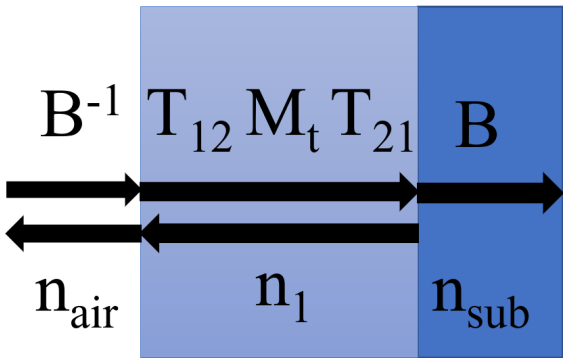

Figure 2.1: A simple transfer matrix problem of a film with refractive index n_1. The effective transfer matrix for this film is described by the sequential product of the paired interface matrices $\mathbf{B}^{-1}\mathbf{T}_{12}$, the in-medium propagation matrix $\mathbf{M}_t$, and the paired interface matrices $\mathbf{T}_{21}\mathbf{B}$.

With layer matrices defined, the transfer matrix method is now a powerful tool. In practice, any one-dimensional structure with layers of constant refractive index can be broken down into a series of layer matrices, and an effective transfer matrix for the entire structure can be defined as the product of these layer matrices. This method can even be used to approximated materials with a graded index of refraction by breaking them down into finite elements, although this is computationally intensive.

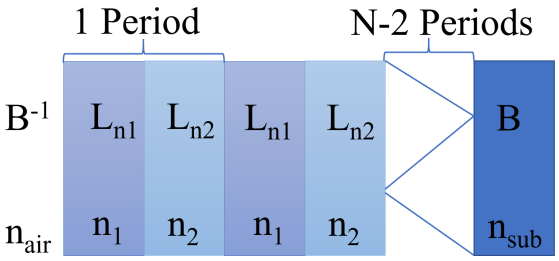

Figure 2.2: The transfer matrix structure of an epitaxially grown bilayer distributed Bragg reflector with N periods.

Consider the case of a simple DBR consisting of alternating layers of material with refractive indexes n_1 and n_2. A single period of this structure may be defined by the product of the layer matrices:

$$\mathbf{L}_{n_1}\mathbf{L}_{n_2} = \mathbf{T}_{n_1}\mathbf{M}_{t_{n_1}}\mathbf{T}_{n_1} * \mathbf{T}_{n_2}\mathbf{M}_{t_{n_2}}\mathbf{T}_{n_2} \tag{2.13}$$

Thus, the effective transfer matrix $\mathbf{M}_{eff}$ for the entire DBR structure is:

$$\mathbf{M}_{eff} = \mathbf{B}^{-1}(\mathbf{L}_{n_1}\mathbf{L}_{n_2})^N\mathbf{B} \tag{2.14}$$

Where N is the number of DBR periods. It is now possible to extract an effective reflectance value that describes the entire structure. Recalling the original definition of the transfer matrix as a relation between wave amplitudes (see Eq. (2.3)), the amplitude reflection coefficient r can be defined as:

$$r = \frac{m_{21}}{m_{11}} \tag{2.15}$$

Where m_{21} and m_{21} are the matrix elements of $\mathbf{M}_{eff}$. The amplitude reflection coefficient is related to the Reflectance R by:

$$R = |r|^2 = |\frac{m_{21}}{m_{11}}|^2 \tag{2.16}$$

The Transmission coefficient T can also be extracted from this matrix [7]:

$$T = |t|^2 = |\frac{m_{11} + m_{21}}{m_{11}}|^2 \tag{2.17}$$

The transfer matrix system can be solved analytically, although in practice it is best to approach the problem numerically, especially since certain material parameters such as index of refraction and length are frequently not constant over the wavelength range of interest.

2.2 Optical Properties of AlGaN alloys

Before attempting to design distributed Bragg reflectors for deep UV optoelectronics, it is necessary to understand the optical behavior of the AlGaN materials system in the UV-C range. Wurtzite-phase aluminum gallium nitride alloys

have bandgaps ranging from 3.42 to 6.2 eV [9]. The band gap does not vary linearly with aluminum content, due to a small bowing parameter. Brunner et al. [9] give the following analytical model for band gap based on Al fraction x_{Al}:

$$E_g(eV) = 6.13x_{Al} + 3.42(1 - x_{Al}) - 1.3x_{Al}(1 - x_{Al}) \tag{2.18}$$

Alternative calculations [10],[11] based on ab initio calculations and later studies have yielded smaller bowing parameters than the 1.3 eV used in Brunner et al.'s model of the bandgap energies. The AlGaN system has a direct band gap over its entire range [11],[12], and so large optical absorption coefficients can be expected above the band edge at any temperature.

The refractive index of AlGaN Alloys is not constant in the deep UV range. As the photon energy of light approaches the bandgap, the refractive index of the material is significantly increased due to a strong excitonic resonance near the band edge [13]. This fact has been exploited to increase the refractive index contrast between AlN and AlGaN films to enhance DBR reflectivity [14]. Brunner et al. [9] again provide an empirical model for the refractive index below the band gap based on photon energy $h\nu$ and Aluminum fraction x:

$$n^2(h\nu, x) = \epsilon(h\nu, x) = C(x) + A(x)y^{-2}(1 - (1 + y)^{1/2} - (1 - y)^{1/2}) \tag{2.19}$$

Where $C(x)$ and $A(x)$ are both functions dependent on the Aluminum fraction and $y = \frac{h\nu}{E_g}$. Brunner et al.[9] found the best fit to data for these two functions was:

$$C(x) = (-2.2 \pm 0.2)x + (2.66 \pm 0.12) \tag{2.20}$$

$$A(x) = (3.17 \pm 0.39)x^{1/2} + (9.98 \pm 0.27) \tag{2.21}$$

This relation does not model behavior of the dielectric function above the bandgap energy E_g, but this area is of little interest for designing DBR structures,

as wavelengths shorter than the bandgap of AlGaN will be strongly absorbed, severely limiting the efficiency of the reflector.

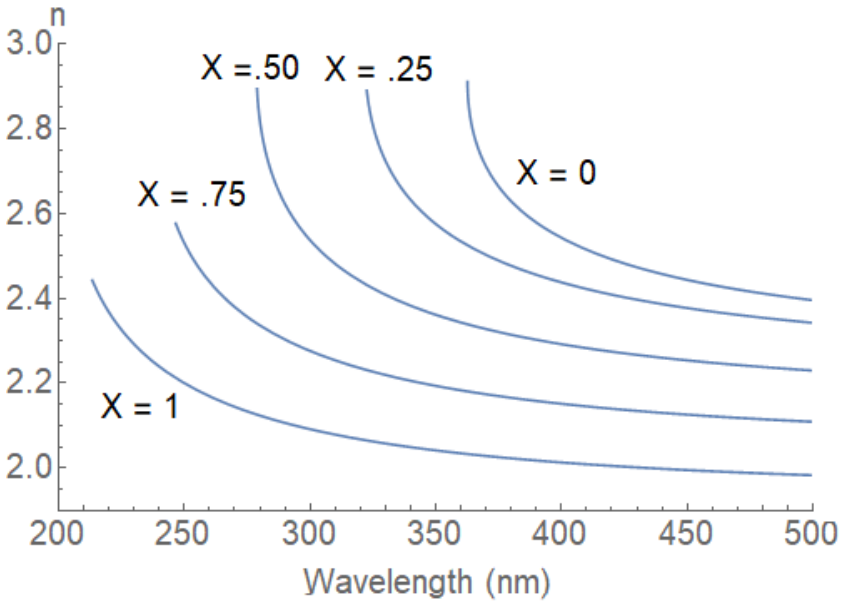

Figure 2.3: The refractive indexes of various AlGaN Alloys with aluminum fraction x in the range from 500 to 200 nm. Each curve terminates approximately at E_g for its respective alloy. Each curve was calculated based on the refractive index model from Brunner et al. [9].

The refractive index contrast between each alloy is fairly low in the visible range, but contrast can be increased near the band edge due to the excitonic resonance peak. This forms the basis of an optimization problem that will be discussed in chapter 3.

2.3 Modeling Absorption in AlGaN DBRs

As with most materials, AlGaN alloys are not completely transparent in the UV-C range. Modeling absorption losses in AlGaN DBRs is critical for understanding the design problems. Absorption can be broadly defined by the Beer-Lambert Law:

$$A(\lambda) = A_0(\lambda)e^{-\alpha(\lambda)D} \tag{2.22}$$

Where α is the absorption coefficient, D is the thickness of the absorbing media, and A_0 and A are the initial and final intensities.

Absorption may be easily integrated with the existing transfer matrix method provided the following assumptions are made:

1. The absorption coefficient of each individual layer is constant throughout the layer.
2. No additional absorption processes occur at the interfaces - i.e. the absorption process is entirely volumetric.

These assumptions are generally acceptable, but due to polarization effects 2D electron and hole gases may form at heterostructure interfaces [1] within AlGaN DBRs, which can increase free-carrier absorption. Thus, this model should be considered most valid for undoped or lightly doped structures, where any absorption effects from 2DEGs or 2DHGs are minimal. If it is assumed that the absorption process is entirely volumetric, then the absorption can be modeled [7] simply by combining the Beer-Lambert Law with the propagation matrix

defined in Equation (2.10):

$$\mathbf{M}_t \equiv \begin{bmatrix} e^{-i(k_n \cdot D)-\alpha D} & 0 \\ 0 & e^{i(k_n \cdot D)-\alpha D} \end{bmatrix} \tag{2.23}$$

This propagation matrix may then be combined with the interface matrices to form the layer matrix as previously demonstrated.

With this model in place, all that is required to model loss in AlGaN layers are functions for the absorption coefficients across the wavelength range of interest. Unfortunately, sub-threshold absorption in wide-band gap semiconductors like AlGaN is a complicated process that depends highly on the growth conditions and defect structure of the individual AlGaN films. Brunner et al. [9] give one of the first empirical models for sub-threshold absorption in AlGaN films:

$$\alpha = \alpha_0 e^{\frac{h\nu}{E_{Urb}}} \tag{2.24}$$

Where E_{Urb} is the energy of the Urbach tail. The Urbach tail is an exponentially increasing absorption coefficient for photon energies below the band gap. This tail is thought to arise from phonon interactions with excitons [15]. Brunner et. al [9] observed that the size of the Urbach energy varied for different AlGaN compositions, from as low as 30 meV for GaN to 230 meV for $Al_{.80}Ga_{.20}N$, before dropping down to around 90 meV for AlN. Brunner et al. further noted that this behavior appeared to correlate with the bowing parameter, as the peak Urbach energy was reached at the same composition that was the furthest from linearity. Alternative data for AlGaN absorption also exists [16], but is incomplete for compositions in the deep UV range with Aluminum fractions above 60 %.

Due to the lack of published data on the absorption coefficients of AlGaN films, it may be productive for any research group interested in DBR growth to

create their own empirical model for AlGaN absorption based on the growth methods and conditions used in their own group.

2.4 Modeling Porous AlGaN Layers

Varying the composition of AlGaN using heterostructures is not the only method that can be used to achieve high refractive index contrast. One commonly used approach to create a larger refractive index contrast is to alter the effective refractive index by increasing the porosity of a layer. Since air has a refractive index of approximately $n_{air} = 1$, contrast induced by layering porous material with solid material can meet or exceed that produced by compositional variation. Porous reflectors have been demonstrated in both indium-tin oxide films [17] as well as GaN epitaxial structures [18].

Most porous material grown at device scale can be assumed to be disordered. Under these conditions, the effective refractive index can be approximated using a simple volume fill model [18]. This model is given by the equation:

$$n_{eff} = ((1 - p)n_{mat}^2 + pn_{air}^2)^{\frac{1}{2}} \tag{2.25}$$

where n_{mat} and n_{air} are the refractive index functions of the material and air, respectively, and p is the fraction of the layer volume occupied by pores. This simple model can also be used to approximate absorption in porous layers:

$$\alpha_{eff} = ((1 - p)\alpha_{mat}^2 + p\alpha_{air}^2)^{\frac{1}{2}} \tag{2.26}$$

However, this approximation is only valid if optical scattering in the porous layer is minimal.

Most disordered porous material can be safely approximated by this volume fill model. Ordered porous material is more difficult, due to the anisotropy of the effective refractive index and effective absorption coefficient. Ordered porous structures thus require individual consideration to model.

2.5 Off-Axis Light Propagation using the Small Angle Approximation

The 1D transfer matrix method described in Section 2.1 is a powerful tool for optical calculations, but it is limited only to analysis on a single optical axis. 2- and 3-dimensional problems rapidly increase the complexity of the problem due to the interference of multiple non-parallel reflection. In general, distributed Bragg reflectors are used on their normal axis, since they are most efficient at normal incidence. However, it may sometimes be useful to consider waves propagating at slight angles to the optical axis of the Bragg reflector. This can be done using the small angle approximation.

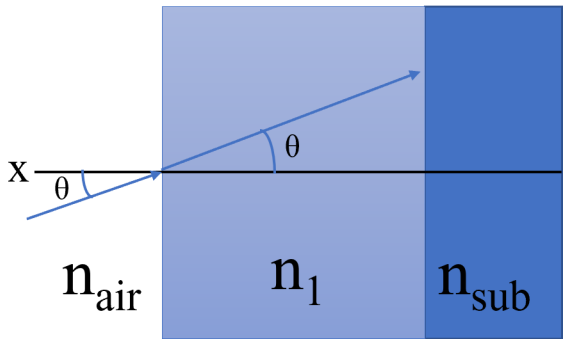

Figure 2.4: A scenario in which light propagates at a small angle $\theta <\approx 10^{\circ}$.

First, consider the two decomposed interface matrices for TE and TM-polarized light, given by equations (2.5) and (2.6). Under the small angle ap-

proximation,

$$cos(\theta) \approx 1 \tag{2.27}$$

and so the form of these matrices is unchanged from equation (2.4). Next, consider the propagation matrix, given by equation (2.10). The distance D_θ that the wave travels through the layer of thickness D is now:

$$D_\theta = Dsec(\theta) = \frac{D}{cos(\theta)} \tag{2.28}$$

While it is possible to further apply the small angle approximation here, this merely yields the same result as on-axis calculations, and therefore it is not instructive to do so. The principle of this approximation is to treat any small variations in angle (under about 10°) as a slight increase in effective layer length. This means that the stopband and reflectivity peak of the mirror will appear red-shifted when measured at a slight angle.

CHAPTER 3

DESIGN PRINCIPLES FOR DEEP UV DISTRIBUTED BRAGG REFLECTORS

3.1 Basics of DBR Design

All distributed Bragg reflectors share some basic design features. DBRs use periodic interface reflections to create a stopband in which forward-propagating light modes are disallowed [19]. Thus, unlike the reflectivity spectrum of a metal mirror, which covers a wide range of wavelengths, the reflectivity spectrum of a DBR is confined to a narrow range of wavelengths. The critical features of this spectrum and their theoretical origins are described below.

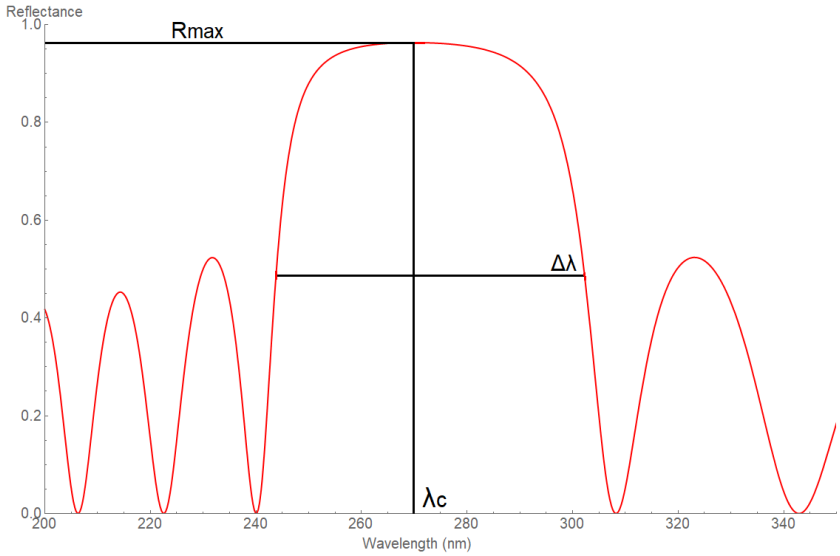

Figure 3.1: Reflectance spectrum of a 10-period UV DBR with center wavelength $\lambda_c = 270\ nm$. The peak reflectivity R_{max} and 3dB stopband width $\Delta\lambda$ are marked on the figure.

The first critical parameter of the DBR spectrum is the center wavelength λ_c. The stopband is formed by constructive interference of reflected waves, so

the center wavelength is determined primarily by the thickness of the structure [20]. To understand this, the conditions for constructive thin film interference at normal incidence are useful:

$$\phi = \pi + 2\pi n \tag{3.1}$$

A 180° phase shift, or some even multiple, is required for complete constructive interference. The simplest way to achieve reflections with phase shifts that are multiples of 180° is to match each layer properly, as shown in Fig. 3.2.

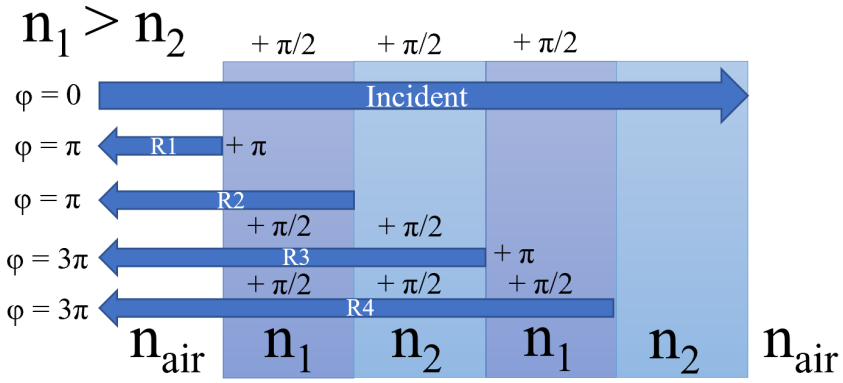

Figure 3.2: A distributed Bragg reflector in which all reflected waves R_n have a phase shift with a multiple of π, leading to constructive interference. Note that an additional phase shift of π is added when transitioning from materials with a lower refractive index to materials with a higher index.

This is the simplest form of DBR, which requires that propagation through each of the layers adds a phase shift $\phi = \frac{\pi}{2}$. Since the incident and reflected waves are modeled as plane waves, this indicates that the thickness D of each layer must be:

$$D = \frac{\lambda_c}{4n} \tag{3.2}$$

Where n is the effective refractive index in the material. This type of DBR is frequently called a "quarter-wave stack" because the length of the layers is equal to a quarter wave in the medium. The quarter-wave DBR is not necessarily the only type of distributed Bragg reflector, since the only requirement to create a

photonic stopband is that constructive interference is maintained. However, the quarter-wave DBR is the most efficient structure [19] if the mirror is designed to reflect a single wavelength. It is worthwhile to note that the effective refractive index of the material affects the central wavelength. This is an important fact for engineering DBRs in the AlGaN system, due to the presence of the excitonic resonance peak in the dielectric function near the band edge.

The second important parameter of a DBR spectrum is the bandwidth of the stopband. The bandwidth of the DBR stopband is principally a function of the refractive index contrast $|n_1 - n_2|$, but various other parameters in real systems such as layer thickness variations can also influence the bandwidth. There is no simple formula to derive the bandwidth of the stopband for any arbitrary DBR structure aside from a complete transfer matrix method simulation. However, for ideal cases of the quarter-wave stack structure described above, an approximation exists[21]:

$$\Delta\lambda \approx \frac{4\lambda_c}{\pi} arcsin\left[\frac{n_1 - n_2}{n_1 + n_2}\right] \tag{3.3}$$

Where λ_c is the central wavelength and $n_1 > n_2$ are the refractive indexes of the alternating layers. This approximation has two caveats: first, it is accurate only where the refractive index is constant or varies slowly. Second, it is only valid for mirrors with a low index contrast [21]. Both of these assumptions may be wrong in the AlGaN system, especially when dealing with porous media. Thus, it is usually better to extract this parameter directly from a transfer matrix simulation fo the device.

The last important parameter of the DBR is the peak reflectivity. The reflectivity of a DBR is primarily a function of the number of periods as well as the refractive index contrast. For an ideal quarter-wave stack DBR, this is the

reflectivity of the center wavelength. As with the stopband width, there is no simple analytical formula for the peak reflectivity of an arbitrary DBR structure. A formula exists for an ideal quarter-wave stack through use of the hyperbolic tangent approximation [22]:

$$R_{max} = \left[\frac{n_0(n_2)^{2N} - n_{sub}(n_1)^{2N}}{n_0(n_2)^{2N} + n_{sub}(n_1)^{2N}}\right]^2 \tag{3.4}$$

Where n_0 and n_{sub} are the refractive indexes of the materials coupling into the DBR on either side, $n_1 > n_2$ are the refractive indexes of the alternating layers, and N is the number of periods in the device. As with the approximation of bandwidth, this approximation is only correct when the contrast between refractive indexes is low and the refractive indexes are constant or slowly varying over the wavelength range of interest. In situations where this isn't true, it is more informative to extract the parameters directly from simulation.

The three critical parameters for DBR design can be summarized as follows:

- Center Wavelength λ_c: Determined primarily by conditions for constructive interference, driven by layer length D and refractive index n.
- Stopband Width $\Delta\lambda$: Determined primarily by refractive index contrast Δn
- Peak Reflectivity R_{max}: Determined primarily by by refractive index contrast Δn and number of periods N.

3.2 Engineering DBRs in the AlGaN System

The AlGaN system does not, at first, appear to be an optimal choice for a DBR structure. The refractive index contrast between aluminum nitride and gallium

nitride is a fairly small $\Delta n \approx .5$ in the visible range, and the contrast between AlGaN alloys and aluminum nitride is even smaller. However, there are several features of the AlGaN system that enable it to be useful as a material for DBRs in the deep UV spectrum:

1. Transparency: AlGaN alloys are wide-bandgap semiconductors with E_g between 3.42 to 6.2 eV. Many oxides used in visible light DBRs such as ITO [17] or TiO_2 [23] have bandgap energies less than 4 eV, making them unsuitable for use in the deep UV spectrum.
2. Conductivity: Unlike most oxides used in DBRs, AlGaN has been successfully n-type doped and has reportedly achieved resistivities as low as $0.026\ \Omega - cm$ [24] even for compositions with an aluminum fraction above 80%. This allows it to potentially be used as a conductor, as in a VCSEL.
3. Manufacturability: Growth techniques for AlGaN layers have been well studied, and using AlGaN DBRs combined with nitride active regions allows devices to be grown epitaxially during the same growth cycle, rather than requiring regrowth on different equipment.

Thus, even a materials system with low refractive index contrast is a useful candidate for a DBR.

One special advantage of working with the AlGaN system is the increased refractive index near the band edge. This is due to an excitonic resonance peak in the dielectric function corresponding to the band gap energy. The refractive index of an AlGaN alloy may increase by as much as .5 for photon energies close to the band gap. Since the peak reflectivity for a given number of periods increases with increasing refractive index contrast, it is possible to significantly

reduce the number of periods in the mirror needed to reach a specific reflectivity.

In a design with no consideration for subthreshold absorption, the greatest refractive index contrast will be reached with a mirror consisting of alternating layers of AlN and the AlGaN composition with a bandgap corresponding to the photon energy of the design wavelength. This minimizes the refraction index of the low-index layers (AlN) and maximizes the index of the high-index (AlGaN) layers. However, this design cannot achieve high reflectivity (> 99 %) in the real world because subthreshold absorption becomes significant. Thus, designing a deep UV DBR requires balancing the increase in contrast with the increase in absorption near the band edge.

To begin this process it is necessary to define the design reflectivity R, and if needed, the design Transmittance T. By simple conservation of energy:

$$R + T + A = 1 \tag{3.5}$$

Where A is the absorbance, which, by the Beer-Lambert law, is equal to:

$$A = \frac{I}{I_0} = e^{-\alpha D} \tag{3.6}$$

For example, it can be seen that 99 % reflective mirror with a 1 % transmittance is physically impossible with a nonzero absorption coefficient. Consider the case of a mirror with $R = 0.99, T = 0.0$. For these conditions, and using the approximation given by eq. (3.4), two relations hold:

$$A = e^{-\alpha_{AlN} D_{AlN} - \alpha_{AlGaN} D_{AlGaN}} = 0.01 \tag{3.7}$$

$$R = \left[\frac{n_0 (n_{AlGaN})^{2N} - n_{sub} (n_{AlN})^{2N}}{n_0 (n_{AlGaN})^{2N} + n_{sub} (n_{AlN})^{2N}} \right]^2 = 0.99 \tag{3.8}$$

Because $R + A = 1$, it is possible to create a system of equations. However, this system is underdefined, so additional constraints must be put into place. The

layer thickness, as in a quarter-wave stack, is defined as

$$D_{AlGaN} = \frac{N\lambda_c}{4n_{AlGaN}} \tag{3.9}$$

This allows the system of equations given by eqs. (3.7) and (3.8) to be solved for n_{AlGaN} and N to generate design curves. The reflectivity in eq. (3.8) approximation can be substituted for the more exact value given by eq. (2.16), but calculating the transfer matrix in this system of equations requires a computationally intensive numerical solution.

One last complication of using the AlGaN system to create DBRs exists. Because AlGaN alloys have a lattice constant that varies significantly from AlN, it is possible that strain relaxation can occur by the formation of cracks if the film is grown too thick. These cracks are undesirable, as they may scatter light and increase subthreshold absorption. The critical thickness for strain relaxation has been calculated [25],[26] to vary from hundreds of nanometers to as low as 40 nm for $Al_{.60}Ga_{.40}N$. In general, if the condition:

$$D_{critical} < \frac{\lambda_c}{4n_{AlGaN}} \tag{3.10}$$

is met, then the DBR is at risk of cracking. This risk is highly dependent on growth conditions and may be exacerbated or improved by different methods of epitaxial growth.

3.3 Rules of Thumb for Compositional and Thickness Variations

Previous sections have considered DBR designs with exact, precise parameters. However, it is nearly impossible to avoid compositional and growth variances

when attempting to grow structures epitaxially. While it is possible to characterize each device and simulate the exact structure, it is often more useful to estimate how variations will affect critical parameters with simple, empirical rules of thumb.

3.3.1 Correlated Thickness Variations

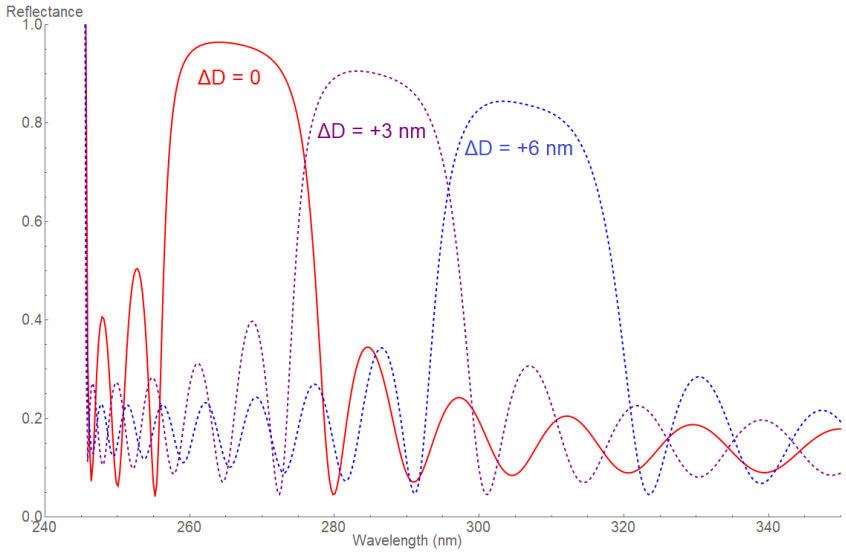

Figure 3.3: Reflectivity spectra for a 20-period 265 nm $Al_{.70}Ga_{.30}N/AlN$ DBR with layer thicknesses $D_{AlGaN} = 27nm$ and $D_{AlN} = 31nm$, with the variation parameter ΔD added to these lengths as a correlated thickness variation.

Underestimating the growth rate of certain layers can cause correlated thickness variations, where all layers are a certain thickness ΔD longer than designed. It can be observed that for small ΔD less than about 10 nm, the redshift in the central wavelength is approximately linear, following the equation:

$$\Delta\lambda_c \approx c_D \Delta D \tag{3.11}$$

Where c_D is a proportional constant for a given wavelength. For a 265 nm mirror, for example, c_D is about 6.67.

3.3.2 Correlated Composition Variations

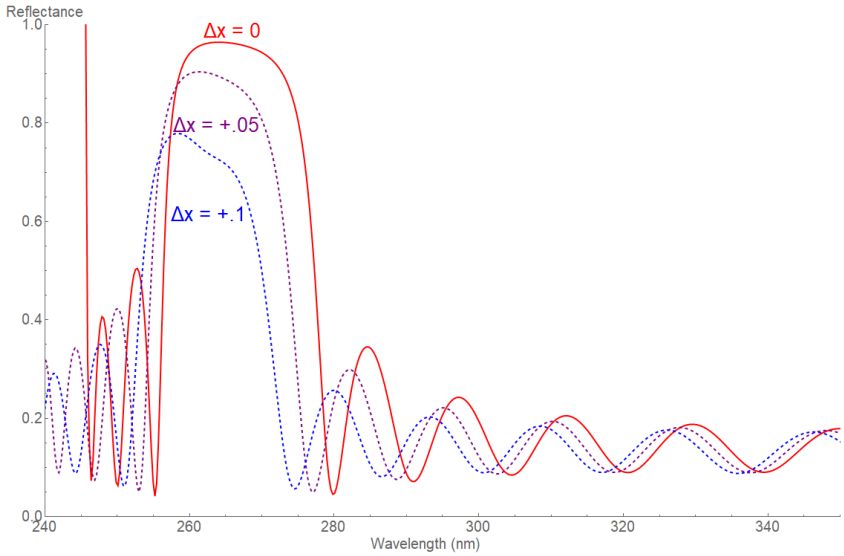

Figure 3.4: Reflectivity spectra for a 20-period 265 nm $Al_{.70+\Delta x}Ga_{.30-\Delta x}N/AlN$ DBR with layer thicknesses $D_{AlGaN} = 27nm$ and $D_{AlN} = 31nm$, with the variation parameter Δx as a correlated compositional variation.

Epitaxial growth of AlN is straightforward, but ensuring the correct composition of a psuedobinary AlGaN alloy is somewhat more difficult. The composition of the alloy may vary by a Δx, such that the alloy is $Al_{X+\Delta x}Ga_{1-X-\Delta x}N$. If this variation is uniform across all layers and not greater than about .1, the blueshift of the central wavelength can be observed to be approximately linear:

$$\Delta\lambda_c \approx -c_x \Delta x \tag{3.12}$$

Where c_x is a proportional constant for a given wavelength. For 265 nm, c_x is approximately equal to 50. It can be seen that small correlated variations in compositions have much less of an effect on center wavelength than correlated length variations.

3.3.3 Uncorrelated Variations

It is difficult to create an all-encompassing rule of thumb for uncorrelated variations because of the various distributions of these errors. It can be reasoned through simple Fourier analysis that if the individual variations δD or δx follow a Gaussian distribution then the shift in center wavelength will be 0, since this indicates that the phase shifts (ϕ) of the reflected waves will also be distributed as a Gaussian. One major issue in considering the approach is that DBRs are not symmetrical structures: The amplitude of the waves reflected by each layer rapidly decrease, as the part of the power of the transmitted wave is reflected at each interface. Thus, any variations in the first few layers the incident beam passes through will have a much greater effect on the reflected power than a variations in layers deeper into the structure.

The approximation given by Eq. (3.4) is a simplified form of the hyperbolic tangent approximation for reflectivity. This widely used approximation is derived from coupled-mode theory [7], and may be re-defined to provide a recursive relation that will prove useful in resolving this issue. The hyperbolic tangent approximation asserts that that, for a quarter-wave reflector with abrupt interfaces [7],

$$r \approx tanh(s_{air} + \frac{2\Delta n}{\lambda} D) \tag{3.13}$$

Where Δn is the difference in refractive index and D is the overall length of the structure. The length of the periods is constant (excluding minor variations) in a quarter-wave stack, so:

$$D = N * (\frac{\lambda_c}{4n_1} + \frac{\lambda_c}{4n_2}) \tag{3.14}$$

Where N is the number of periods in the reflector. With the length now exactly defined, it is easy to define the fractional component that each additional period

The fractional component of reflectivity can be defined recursively:

$$r_{frac}(\lambda_c, N) \approx tanh(s_{air} + \frac{2\Delta n}{\lambda} N * (\frac{\lambda_c}{4n_1} + \frac{\lambda_c}{4n_2})) - r_{frac}(\lambda_c, N-1) \tag{3.15}$$

In this case, the first fractional component $r_{frac}(\lambda_c, 0)$ is simply the reflectivity of the first interface- the surface, given by the Fresnel equations (2.1),(2.2). We can now insert uncorrelated variances in length δd and composition δn into each expression.

$$r_{frac}(\lambda_c, N) \approx tanh(s_{air} + \frac{2\Delta n}{\lambda} N * (\frac{\lambda_c}{4(n_1 \pm \delta n_1)} \pm \delta d_1 + \frac{\lambda_c}{4(n_2 \pm \delta n_2)} \pm \delta d_1)) - r_{frac}(\lambda_c, N-1) \tag{3.16}$$

It can be understood from this expression that the individual variances will have a very different effect at the beginning of the stack than at the end of the stack, since the error components in the initial layers will propagate through the recursion. Importantly, the upper bound for the variance caused by a single layer is equivalent to $\left|r_{frac}\right|$ for that same layer- as in the limiting case, the error is only so large as to create a 90 degree phase shift for the reflected wave, resulting in total destructive interference of the reflected wave. Since the fractional component of the reflectivity is high only for the first few layers of the stack, compositional and length variations in these layers are responsible for most of the variance in the reflectivity.

A good approximation of the reflectivity variance can be made if it is assumed that all variations in length and composition are approximately equal in magnitude. In this case, the known variance in composition or length of the first layer (or first few layers, averaged) is substituted into the correlated variation cases discussed in the previous two sections. Since each subsequent layer reflects less light than the first, the magnitude of the first error (or first few errors) can be assumed to dominate.

3.4 Incorporating Porous Layers

Porous layers can greatly decrease the effective index of refraction, but there are several practical concerns that must be addressed before they can be incorporated into a DBR design. Porous layers are typically achieved by a selective electrochemical etch [18], which takes advantage of differential n-type doping to partially etch these layers. Ideally, an etch that selectively etches away AlN layers while leaving AlGaN layers intact would achieve greatest contrast, since the AlGaN layers naturally have a higher index of refraction. However, bandgap selective photoelectrochemical etches [27] can only etch AlGaN from AlN. Doping-selective electrochemical etches are restricted by similar issues, since the polarization effect in AlN/AlGaN heterostructures [1] will cause most electrons to form a 2DEG at the AlGaN/GaN interface. In this case, it is simpler to use a single composition, such as AlN, and use modulated doping to achieve the selective etch.

Beyond material selection, there are certain obvious limitations to the design of DBRs with porous layers. For example, layers with porosity greater than about 80 % will be a major device stability concern. Any internal stresses in the layer will be magnified due to the small amount of material remaining. Layers with porosity under 20 % will require an impractically large number of periods to achieve high reflectivity due to the very small refractive index contrast. Finally, all DBRs based on porous material may experience scattering effects due to the random distribution of the voids in the material. This may render porous materials unsuitable for applications requiring very high reflectivity.

3.4.1 Correlated Porosity Variation

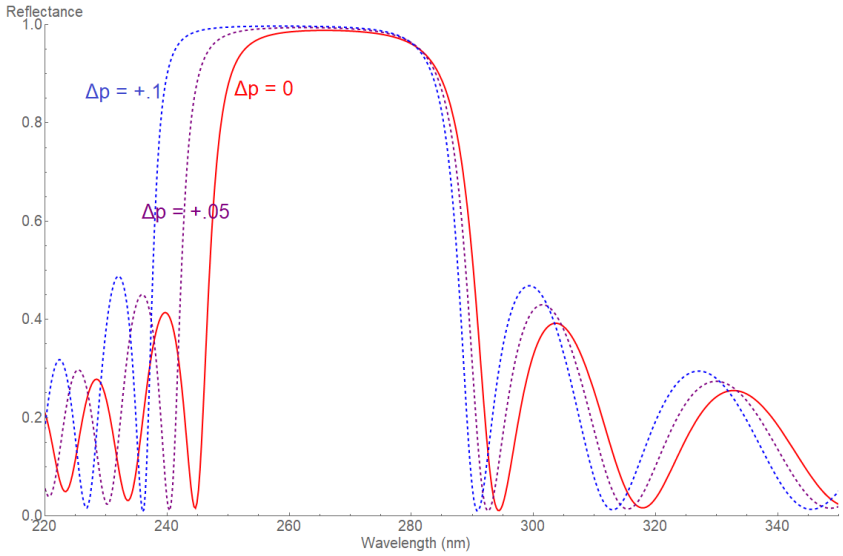

Figure 3.5: Reflectivity spectra for a 10-period, 265 nm porous AlN/AlN$_p$ DBR with layer thicknesses $D_{AlN_p} = 39.4nm$ and $D_{AlN} = 31nm$, with the variation parameter Δp as a correlated compositional variation.

As with the composition Δx and layer thickness ΔD, it is helpful to define a porosity variation Δp caused by over- or underestimation of the etch rate during the electrochemical etch of a porous DBR. If the variation in porosity is small (under 10 %), then the shift in central wavelength is approximately linear:

$$\Delta\lambda_c \approx -c_p \Delta p \tag{3.17}$$

Where c_p is a proportional constant at a certain wavelength. For this 265 nm DBR, c_p is approximately 66.

CHAPTER 4

EPITAXIAL GROWTH OF DEEP UV DISTRIBUTED BRAGG REFLECTORS AND CHARACTERIZATION METHODS

4.1 Molecular Beam Epitaxy

Although many methods are available to epitaxially grow AlGaN films, the two most frequently used for modern device research are Metal Organic Chemical Vapor Deposition (MOCVD) and Molecular Beam Epitaxy (MBE). Both MOCVD [28],[29] and MBE [14],[30],[31] have been used to grow AlGaN distributed Bragg reflectors. This thesis will focus on the latter of the two methods, since MBE offers certain advantages for device growth, such as the ability to incorporate magnesium-doped P-type layers anywhere in the device geometry without risk of hydrogen passivation.

Molecular Beam Epitaxy is essentially a highly-regulated thermal evaporation process that takes place at ultra-high vacuum conditions (chamber pressures of 10^{-9} Torr or lower) and very slow growth rates (frequently measured in nanometers per minute) [32]. At these low pressures, the mean free path of evaporated atoms can be measured in meters, forming atomic ”beams” that travel directly to a target substrate. If the target substrate is heated, atoms arriving at the surface may have enough energy to become adsorbed and then form bonds with the surface. By controlling growth conditions precisely, flow of the adsorbed atoms on the surface will cause them to migrate to sites located at the edge of atomic steps at the surface, allowing them to expand the crystal epitaxially monolayer-by-monolayer. Any atoms from the impinging beams that do not stick to the substrate (or miss) will either stick to the vacuum chamber

walls or be pumped out of the system. This allows the growth of semiconductor heterostructures that are sharply defined and relatively free of contamination.

The core of an MBE system is the growth chamber. The growth chamber consists of three primary components:

- Effusion cells - These are specially designed thermal evaporators (typically Knudsen Cells [33]) filled with solid-phase source elements. The geometry of the cells is specially designed to produce a conical beam aimed at the substrate mount. Effusion cells are covered with specialized shutters that can rapidly block the beam to terminate growth.
- Substrate mount - A rotating mount for crystalline substrates. The mount contains a thermocouple and heater unit designed to keep the substrate at the elevated temperatures needed for crystal growth. The mount is designed to rotate to ensure even growth over the entire substrate and so that RHEED can be used to monitor growth.
- RHEED and other sensors - Reflection High Energy Electron Diffraction (RHEED) is a type of *in situ* measurement technique used to characterize and control epitaxial growth. Similar to X-ray diffraction, RHEED uses the diffraction pattern created by a high-energy electron beam grazing the substrate to monitor the monolayer growth [34]. As atomic steps form on the surface, the intensity of the diffracted electron beam is reduced due to diffuse scattering from the atomic steps, but returns to its original intensity when the monolayer is complete. These oscillations can be used to characterize the growth rate and surface quality in real time [35]. Other types of sensors such as spectroscopic ellipsometers [36] and laser reflectometers [37] have also been used to make up for shortcomings in RHEED

techniques.

Growth of the III-V nitrides in an MBE system requires some special considerations. As nitrogen is a gas at room temperature, it cannot be delivered to the surface of a substrate via an effusion cell as aluminum and gallium can. Instead, an energetic nitrogen plasma must be introduced into the chamber to produce a nitrogen species reactive enough to form bonds with the adsorbed aluminum and gallium atoms [38]. An MBE System containing a plasma source is known as a Plasma-assisted Molecular Beam Epitaxy (PAMBE) system. In AlGaN MBE growth, the power delivered to the nitrogen source is one of the critical variables used to control growth rates.

4.2 Epitaxial Growth of AlGaN Distributed Bragg Reflectors

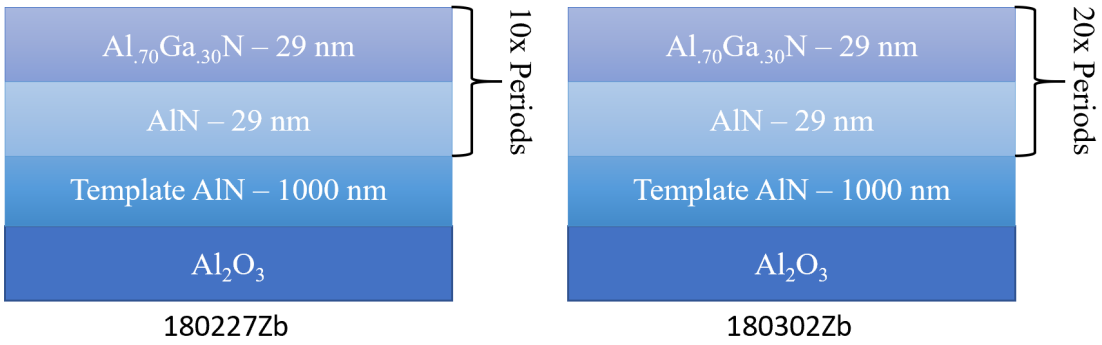

Figure 4.1: Two DBR designs used in experimental MBE growth. Both structures used alternating 29 nm layers of AlN and $Al_{.70}Ga_{.30}N$ for simplicity. The second structure was grown at a faster growth rate to enable efficient growth of 20 periods.

To confirm the validity of the model and designs discussed in Chapters 2 and 3, a Veeco Gen10 Plasma-assisted Molecular Beam Epitaxy system was used to grow two simple AlGaN distributed Bragg Reflectors. The design of these Bragg

reflectors (see fig. 4.1) is approximately that of a quarter-wave stack using AlN and $Al_{.70}Ga_{.30}N$, although the design has intentionally lengthened the sections of $Al_{.70}Ga_{.30}N$ to be identical in length to the AlN sections. This allowed superlattice measurements using X-ray Diffraction to be taken more easily, although this design choice degrades the quality of the reflector. Basic physical statistics of the designs can be found in Table 4.1 :

Sample Name	λ_c (nm)	x_{Al}	D_{AlN} (nm)	D_{AlGaN} (nm)	N
180227Zb	265	.70	29	29	10
180302Zb	265	.70	29	29	20

Table 4.1: Physical dimensions and design parameters of the two DBR designs chosen for MBE growth.

The choice of substrate was a pair of 0.5 cm x 0.5 cm sapphire (Al_2O_3) wafers with a pre-grown AlN template from Dowa Electronic Materials Co. This was due to the expense of obtaining bulk AlN substrates; AlN template wafers offer acceptable growth characteristics and optical properties for the purposes of the study.

Growth of the first sample (180227Zb) began with a nitrogen RF plasma power of 200 W. This was on the lower end of the range of feasible plasma power, and was chosen because it had shown the potential for smooth interfaces during earlier growths on the same system. However, the 200 W power only achieved a growth rate of approximately 4.5 nm/min, meaning that growth of a 20-period reflector would take upwards of 8 hours to complete. This was not considered feasible for long period growth. Additionally, Migration-enhanced epitaxy (MEE) was used to grow the AlN layers. This process temporarily blocks the Aluminum beam so that excess adsorbed aluminum on the epitaxy surface can be consumed [39]. This is intended to result in reduced surface

roughness. Aluminum and nitrogen were deposited in 60 second increments, then the aluminum shutter was closed, while the nitrogen plasma source remained active for 6 additional seconds.

More complete growth conditions for the first growth are listed in Table 4.2:

Layer	T_{sub} ($^{\circ}C$)	P_{N_2} (W)	T_{Al} ($^{\circ}C$)	T_{Ga} ($^{\circ}C$)	N_2 Flow Rate (sccm)
AlN	750	400	1115	Shutter Closed	1.8
$Al_{.70}Ga_{.30}N$	750	400	1099	1005 (905*)	1.8

Table 4.2: MBE growth parameters for the growth of Sample 180227Zb on a Veeco Gen10 MBE system. Includes Substrate thermocouple temperature, Plasma power, Cell temperatures, and Nitrogen flow rate.
*The thermocouple for the Gallium cell is believed to read about 100 $^{\circ}C$ lower than temperature at the cell's tip.

While growth under these conditions was successful, it would take too long to grow the 20- and 30-period distributed Bragg reflectors needed to achieve reflectivity above 99 %. The growth parameters were recalculated and cell temperatures increased to increase atomic flux to that necessary for a plasma power of 400 W. This vastly increased the growth rate so that a 20-period DBR could be grown in about 4 hours. A second sample, the 20-period DBR 180302Zb, was grown with these recalculated parameters. As before, an MEE strategy was used for the AlN layers, with an interruption period of about 10 seconds. More comprehensive data is shown in Table 4.3:

Layer	T_{sub} ($^{\circ}C$)	P_{N_2} (W)	T_{Al} ($^{\circ}C$)	T_{Ga} ($^{\circ}C$)	N_2 Flow Rate (sccm)
AlN	750	200	1083	Shutter Closed	1.8
$Al_{.70}Ga_{.30}N$	750	200	1063	980 (880*)	1.8

Table 4.3: MBE growth parameters for the growth of Sample 180302Zb on a Veeco Gen10 MBE system. Includes Substrate thermocouple temperature, Plasma power, Cell temperatures, and Nitrogen flow rate.
*The thermocouple for the Gallium cell is believed to read about 100 $^{\circ}C$ lower than temperature at the cell's tip.

The second growth strategy proved to be more effective, as the 20-period DBR was shown to have the proper stopband width and central wavelength, while the 10-period DBR could not be found to have any noticeable stopband, possibly due to strong subthreshold optical absorption.

4.3 Structural Characterization Methods

Although MBE provides several *in situ* methods (such as RHEED) for characterizing the structure of epitaxially grown films, it does not provide a comprehensive picture of the structure. It is often necessary to use other analysis methods to characterize the structure and ensure that it matches theoretical specifications before comparing performance. Two of the most useful structural characterization methods for DBR growth are X-ray Diffraction (XRD) and Atomic Force Microscopy (AFM).

4.3.1 X-ray Diffraction

X-ray diffraction is one of the most common methods of analysis used for thin films. X-ray diffraction relies on the fact that atomic planes are regularly spaced in crystals and thus act as Bragg gratings for X-rays. X-ray diffraction can therefore be used to determine the spacing of the planes, and consequently be used to estimate the true composition of psuedobinary alloys like AlGaN. The quality of the grown crystal can also be inferred from the XRD spectrum, since crystals with poor quality will not diffract as strongly as perfect crystals and may cause secondary diffraction peaks. The theory of simulating complex thin-film struc-

tures such as DBR is too involved to be examined in depth here and is best left to a more comprehensive introductory text such as Fewster (1996) [40].

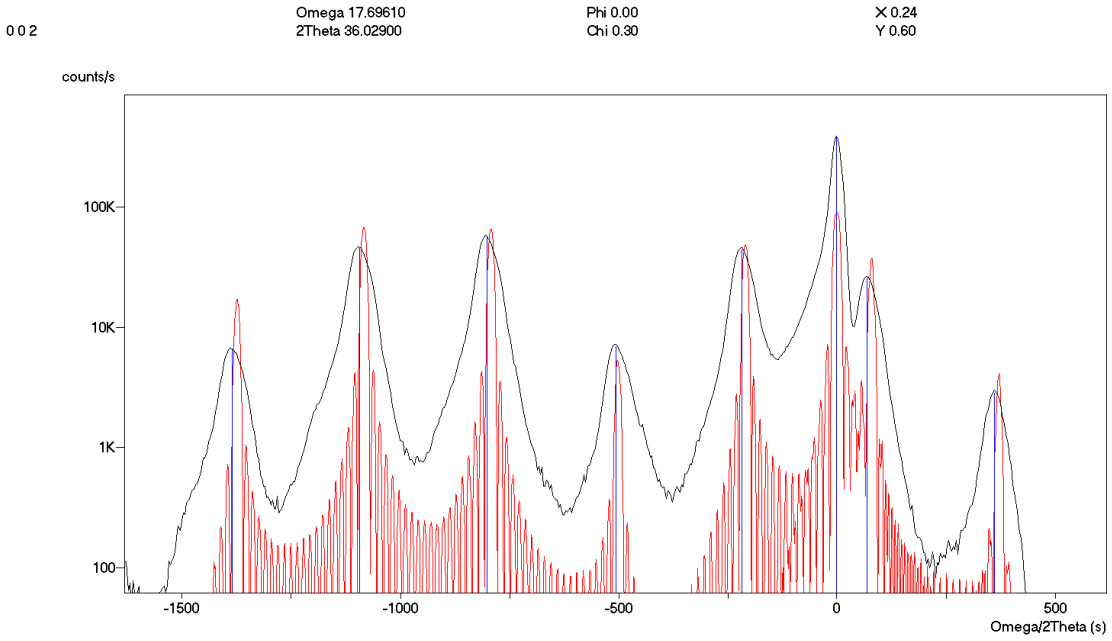

Figure 4.2: The $\Omega/2\theta$ spectrum of 20-Period DBR 180302Zb focused around the 0 0 2 diffraction peak. The red lines show a simulated XRD spectrum based on an AlGaN/AlN DBR.

X-ray diffraction can also be used to characterize larger structures like the DBR superlattice [41]. This measurement is especially useful in a DBR as a way of confirming that the layers have been grown to the proper thickness. Superlattice satellite fringe measurement of the 20-period DBR 180302Zb showed a layer thickness of 29 nm - exactly in line with the intended design. In this way, X-ray diffraction is an effective diagnostic tool for ensuring layer thicknesses, alloy compositions, and crystal quality all satisfy the design requirements of the DBR.

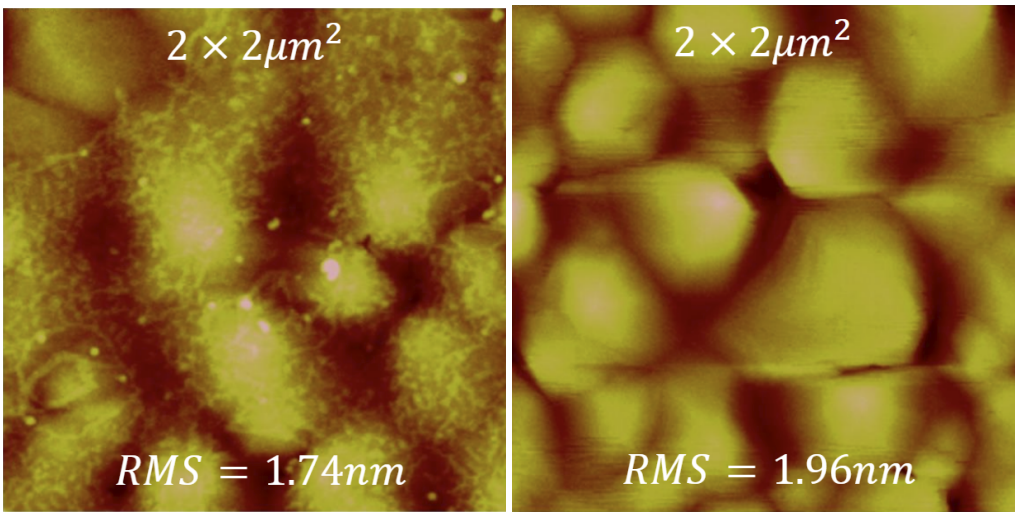

Figure 4.3: *Left:* An AFM micrograph showing the variations on the surface of 10-period DBR 180227Zb.
Right: An AFM micrograph of the surface of 20-period DBR 180302Zb.

4.3.2 Atomic Force Microscopy

Atomic force microscopy is a useful tool for analyzing the surface morphology of MBE grown films. AFM works by scanning a nano-sized probe tip over the surface of the material, then measuring the deflection of the probe tip at each point. In this way it is able to create a topographical map of the surface. Statistics from this topographical map can be used to determine the surface roughness. On very smooth films, atomic steps can even be visually identified in AFM micrographs.

Rough interfaces are undesirable for distributed Bragg reflector, as they can scatter light in ways that do not contribute constructive interference to the reflected wave, limiting the efficiency of the reflector. The two MBE grown DBR samples (seen in Fig. 4.3) have somewhat rough surfaces, with a root mean square variation greater than 1 nm over a 2 x 2μm zone. This may be the cause of the reduced reflective efficiency as compared to theory.

4.4 Optical Characterization Methods

While structural characterizations are useful for diagnosing problems with the epitaxial growth process, the ultimate test of a distributed Bragg reflector is its optical performance. If the DBR is only intended to be used as a mirror, the reflectance spectrum is the most important benchmark.

4.4.1 Absolute Specular Reflectance Spectroscopy

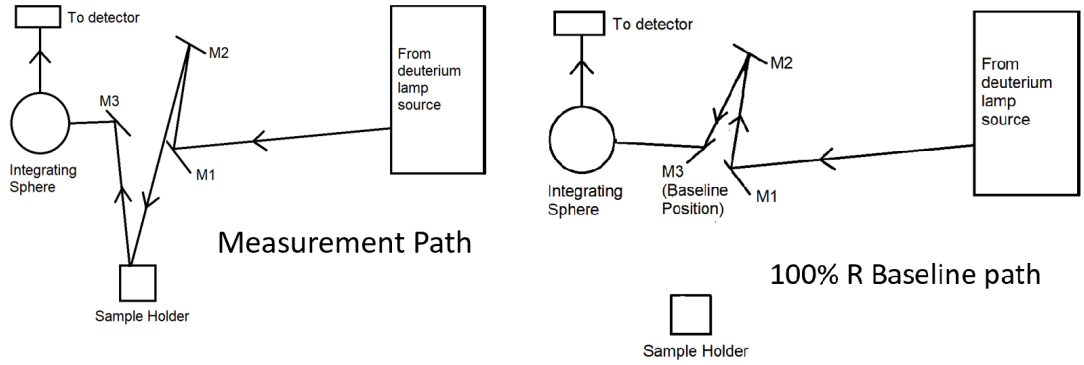

Figure 4.4: *Left:* The measurment pathway for an absolute specular reflection using sequential mirrors.
Right: The 100 %R baseline pathway that bypasses the sample mirror.

Measuring the reflectance spectrum of a distributed Bragg reflector tuned to reflect in the deep UV spectrum is more difficult than most reflectance measurements. Unlike the visible range, there are few reference mirrors that can be used, since most metals will absorb light in this range. Additionaly, diffuse reflective materials used in integration spheres (such as Spectralon [42]) will also perform poorly in the deep UV range. This means that simple total reflectance measurements using UV-visible light spectrometers with integration spheres can give inaccurate results. Additionally, only the specular reflectance of light is a con-

cern in distributed Bragg reflectors, since light scattered in any other direction will be lost in a real device.

Absolute specular reflectance spectroscopy is a technique designed to overcome these difficulties. Rather than the sample being referenced to some mirror with a known spectrum, the sample is inserted into a chain of mirrors that form a pathway between a spectral source and a detector. These mirrors can be treated as a one-dimensional optical system, and ordinarily have the transfer matrix structure:

$$\mathbf{M}_{sum} = \mathbf{M}_1\mathbf{M}_2\mathbf{M}_3\mathbf{M}_4 \ \ etc. \tag{4.1}$$

An absolute specular reflectance measurement system will have a pair of movable mirrors that will alter the path of the optical beam so the sample acts as a mirror in the chain. Thus, the transfer matrix becomes:

$$\mathbf{M}_{sum} = \mathbf{M}_1\mathbf{M}_2\mathbf{M}_{sample}\mathbf{M}_3\mathbf{M}_4 \ \ etc. \tag{4.2}$$

In this case, the specular reflectance of the sample can be defined simply as the intensity (Transmittance) of the beam that is diverted to reflect off the sample divided by the Transmittance of the original path, which represents 100 % R. In this way, the system avoids the collection of diffuse reflection and the other mirrors do not alter the result, as any losses are accounted for in both pathways.

The absolute specular reflectance spectrum of the MBE grown DBRs 180227Zb (10-period) and 180302Zb (20-period) shows some interesting results. Although 180302Zb has a stopband and center wavelength very close to what is predicted by simulation, it has a very low reflectivity, peaking at around 44 % instead of 90 %. This may be due to imperfections or excessive subthreshold absorption. 180227Zb barely appears to have a stopband due to its reflectivity

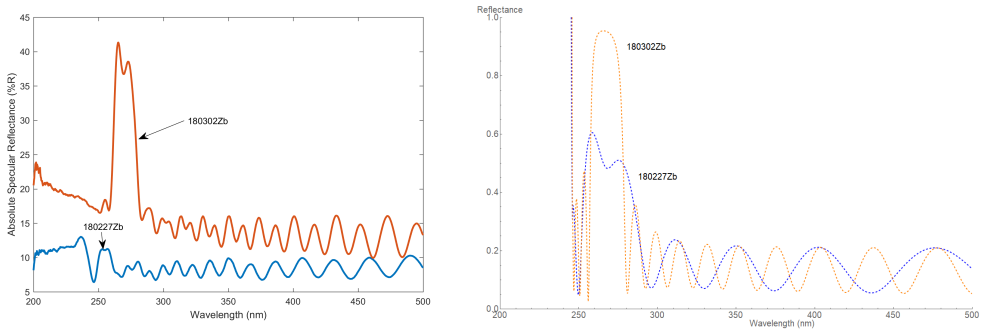

Figure 4.5: *Left:* Absolute specular reflectance spectra for both MBE grown DBRs *Right:* Simulated reflectance spectra for both MBE grown DBRs.

barely exceeding the higher-order fringes. Both reflectors show much lower reflectivity than expected, which may indicate unexpected losses in the absolute specular reflectance measurement as an alternative explanation.

Although it is possible to perform absolute specular reflectance measurements using a series of different mirrors (as was done to generate the spectra for the MBE grown samples in Fig. 4.5), A better controlled method is to use repeated reflections off of the same two mirrors. This method was demonstrated by Berseth et al. [43]. Alternatively, the absolute specular reflectance may be measured by the cavity phase-shift method [44], which measures phase shifts in a resonant cavity caused by absorption losses. Both of these methods have advantages and disadvantages: the ”Z” method used by Berserth et al. places restriction on sample geometry, while the cavity phase-shift method demands very high reflectivity to work effectively.

CHAPTER 5

CONCLUSIONS

5.1 Status of Model Verification

The optical system model of an AlGaN/AlN distributed Bragg reflector presented in chapter 2 of this thesis was combined with the design priciples for DBRs presented in chapter 3 to create the designs for the two MBE-grown DBRs presented in chapter 4 of this thesis. However, the results of these growths have been mixed. While the model presented was able to correctly predict the center wavelength and stopband width of a real AlGaN/AlN DBR, it was not able to accurately predict the maximum reflectivity of the grown mirrors. Naturally, this leads to the question of "Why?". An accounting of the assumptions is in order.

In defining the transfer matrix method, it was assumed that interfaces were perfectly flat and abrupt, and that absorption, if it occured, was an entirely volumetric process that took part across the entire crystal. However, as AFM images reveal (see fig. 4.3), the surface of the crystal was not completely flat. While features only 2 nm in height are not enough to cause significant diffuse scattering, they are still capable of causing minor phase shifts that could degrade the maximum reflectivity of the reflector. This calls forward a greater issue- the 1D transfer matrix method has no adequate treatment for the issue of minor dimensional variances aside from attempts to apply variational methods to address this problem.

The over-reliance on the use of the Brunner et al. [9] models of AlGaN optical

constants may be causing errors to persist in the simulation. It must be noted that some of Brunner et al.'s observations, such as the AlGaN bowing parameter of +1.3 eV, have been called into question by other measurements [11]. The lack of any alternate empirical models for the optical constants of AlGaN may be a previously unidentified impediment into the simulation of AlGaN structures.

Despite these flaws, the model still holds some value. It was able to correctly inform the design of a (non-optimized) Distributed Bragg Reflector that worked well enough to be seen easily even with uncalibrated growth conditions. Parts of the model remain completely unverified, such as the adaptations used to treat Porous layers. This is driven by a lack of technical capacity, as no procedures to reliably create porous AlGaN or AlN layers have yet been established. These areas remain promising for future research.

APPENDIX A

COMMON ABBREVIATIONS AND SYMBOLS

A	Absorbance
AlN	Aluminum Nitride
AlGaN	Aluminum Gallium Nitride
DBR	Distributed Bragg Reflector
E_g	Bandgap Energy
MBE	Molecular Beam Epitaxy
MEE	Migration Enhanced Epitaxy
PAMBE	Plasma Assisted Molecular Beam Epitaxy
R	Reflectance
RHEED	Reflection High-Energy Electron Diffraction
T	Transmittance
UV	Ultraviolet Light
UV-C	Ultraviolet Light between 200 nm - 300 nm
VCSEL	Vertical Cavity Surface Emitting Laser

BIBLIOGRAPHY

[1] J. Simon, V. Protasenko, C. Lian, H. Xing, and D. Jena, "Polarization-induced hole doping in wide-band-gap uniaxial semiconductor heterostructures.," *Science (New York, N.Y.)*, vol. 327, no. 5961, pp. 60–4, 2010.

[2] M. Kneissl, T. Kolbe, C. Chua, V. Kueller, N. Lobo, J. Stellmach, A. Knauer, H. Rodriguez, S. Einfeldt, Z. Yang, N. M. Johnson, and M. Weyers, "Advances in group III-nitride-based deep UV light-emitting diode technology," *Semiconductor Science and Technology*, vol. 26, no. 1, p. 014036, 2011.

[3] S. M. Islam, V. Protasenko, H. G. Xing, and D. Jena, "250 nm Deep UV LED Using GaN / AlN Heterostructures On Bulk AlN Substrates," in *CLEO: Science and Innovations 2016*, vol. 4, pp. 5–6, 2016.

[4] Z. Bryan, I. Bryan, R. Kirste, R. Collazo, and Z. Sitar, "Status and challenges in deep UV semiconductor lasers," in *TuB1.3 (Invited)*, vol. 3, pp. 123–124, 2015.

[5] H.-Y. Lin, K.-J. Chen, S.-W. Wang, C.-C. Lin, K.-Y. Wang, J.-R. Li, P.-T. Lee, M.-H. Shih, X. Li, H.-M. Chen, and H.-C. Kuo, "Improvement of light quality by DBR structure in white LED," *Optics Express*, vol. 23, no. 3, p. A27, 2015.

[6] J. Hong, W. Huang, and T. Makino, "On the transfer matrix method for distributed-feedback waveguide devices," *Journal of Lightwave Technology*, vol. 10, no. 12, pp. 1860–1868, 1992.

[7] H. K. H. Choy, *Design and Fabrication of Distributed Bragg Reflectors for Vertical-Cavity Surface-Emitting Lasers*. Masters thesis, Massachusetts Institute of Technology, 1998.

[8] E. X. Perez, *Design, fabrication and characterization of porous silicon multilayer optical devices*. PhD thesis, Universitat Rovira I Virgili, 2007.

[9] D. Brunner, H. Angerer, E. Bustarret, F. Freudenberg, R. Höpler, R. Dimitrov, O. Ambacher, and M. Stutzmann, "Optical constants of epitaxial AlGaN films and their temperature dependence," *Journal of Applied Physics*, vol. 82, no. 10, pp. 5090–5096, 1997.

[10] R. R. Pelá, C. Caetano, M. Marques, L. G. Ferreira, J. Furthmüller, and L. K. Teles, "Accurate band gaps of AlGaN, InGaN, and AlInN alloys calcula-

tions based on LDA-1/2 approach," *Applied Physics Letters*, vol. 98, no. 15, 2011.

[11] I. Vurgaftman and J. R. Meyer, "Band parameters for nitrogen-containing semiconductors," *Journal of Applied Physics*, vol. 94, no. 6, pp. 3675–3696, 2003.

[12] F. Litimein, B. Bouhafs, Z. Dridi, and P. Ruterana, "The electronic structure of wurtzite and zincblende AlN: An ab initio comparative study," *New Journal of Physics*, vol. 4, 2002.

[13] J. Wagner, H. Obloh, M. Kunzer, M. Maier, K. Köhler, and B. Johs, "Dielectric function spectra of GaN, AlGaN, and GaN/AlGaN heterostructures," *Journal of Applied Physics*, vol. 89, no. 5, pp. 2779–2785, 2001.

[14] T. Detchprohm, Y. S. Liu, K. Mehta, S. Wang, H. Xie, T. T. Kao, S. C. Shen, P. D. Yoder, F. A. Ponce, and R. D. Dupuis, "Sub 250 nm deep-UV AlGaN/AlN distributed Bragg reflectors," *Applied Physics Letters*, vol. 110, no. 1, 2017.

[15] H. Sumi and A. Sumil, "The Urbach-Martienssen Rule Revisited," *Journal of the Physical Society of Japan*, vol. 56, no. 6, pp. 2211–2220, 1987.

[16] J. F. Muth, J. D. Brown, M. A. L. Johnson, Z. Yu, R. M. Kolbas, J. W. Cook, and J. F. Schetzina, "Absorption Coefficient and Refractive Index of GaN, AIN and AlGaN Alloys," *MRS Proceedings*, vol. 537, no. January 1999, p. G5.2, 1999.

[17] M. F. Schubert, J. Q. Xi, J. K. Kim, and E. F. Schubert, "Distributed Bragg reflector consisting of high- and low-refractive-index thin film layers made of the same material," *Applied Physics Letters*, vol. 90, no. 14, pp. 88–91, 2007.

[18] C. Zhang, S. H. Park, D. Chen, D. W. Lin, W. Xiong, H. C. Kuo, C. F. Lin, H. Cao, and J. Han, "Mesoporous GaN for Photonic Engineering-Highly Reflective GaN Mirrors as an Example," *ACS Photonics*, vol. 2, no. 7, pp. 980–986, 2015.

[19] B. Osting, "Bragg structure and the first spectral gap," *Applied Mathematics Letters*, vol. 25, no. 11, pp. 1926–1930, 2012.

[20] M. Lapp, *Deposition and Characterization of Dielectric Distributed Bragg Reflectors*. Masters thesis, Chalmers University of Technology, 2016.

[21] C. Alhenc-Gelas, P. Heroin, M. Abid, J. Jacquet, S. Gautier, and A. Ougazzaden, "Design rules of high reflectivity Bragg GaAlN mirrors for 300 nm VCSELs," *Proceedings of the SPIE - The International Society for Optical Engineering*, vol. 7229, no. 1, p. 72290N (12 pp.), 2009.

[22] C. J. R. Sheppard, "Approximate calculation of the reflection coefficient from a stratified medium," *Pure and Applied Optics: Journal of the European Optical Society Part A*, vol. 4, no. 5, pp. 665–669, 1995.

[23] J. W. Leem, X.-Y. Guan, and J. S. Yu, "Tunable distributed Bragg reflectors with wide-angle and broadband high-reflectivity using nanoporous/dense titanium dioxide film stacks for visible wavelength applications," *Optics Express*, vol. 22, no. 15, p. 18519, 2014.

[24] F. Mehnke, T. Wernicke, H. Pingel, C. Kuhn, C. Reich, V. Kueller, A. Knauer, M. Lapeyrade, M. Weyers, and M. Kneissl, "Highly conductive n-AlxGa1-xN layers with aluminum mole fractions above 80%," *Applied Physics Letters*, vol. 103, no. 21, pp. 1–4, 2013.

[25] R. A. Coppeta, H. Ceric, D. Holec, and T. Grasser, "Critical thickness for GaN thin film on AlN substrate," in *IEEE International Integrated Reliability Workshop Final Report*, no. 2, pp. 133–136, 2013.

[26] K. Ding, V. Avrutin, Ü. Özgür, and H. Morkoç, "Status of Growth of Group III-Nitride Heterostructures for Deep Ultraviolet Light-Emitting Diodes," *Crystals*, vol. 7, no. 10, p. 300, 2017.

[27] J. Grenko, C. Reynolds Jr, R. Schlesser, K. Bachmann, Z. Rietmeier, R. F. Davis, and Z. Sitar, "Selective Etching of GaN from AlGaN / GaN and AlN / GaN," *MRS Internet Journal of Nitride Semiconductor Research*, vol. 9, no. 5, p. 1, 2004.

[28] X. L. Ji, R. L. Jiang, B. Liu, Z. L. Xie, J. J. Zhou, L. Li, P. Han, R. Zhang, Y. D. Zheng, and J. G. Zheng, "Structural characterization of AlGaN/AlN Bragg reflector grown by metalorganic chemical vapor deposition," *Physica Status Solidi (a)*, vol. 205, no. 7, pp. 1572–1574, 2008.

[29] Y. S. Liu, S. Wang, H. Xie, T. T. Kao, K. Mehta, X. J. Jia, S. C. Shen, P. D. Yoder, F. A. Ponce, T. Detchprohm, and R. D. Dupuis, "Strain management

of AlGaN-based distributed Bragg reflectors with GaN interlayer grown by metalorganic chemical vapor deposition," *Applied Physics Letters*, vol. 109, no. 8, 2016.

[30] A. R. Getty, A. David, Y. Wu, C. Weisbuch, and J. S. Speck, "Demonstration of distributed Bragg reflectors for deep ultraviolet applications," *Japanese Journal of Applied Physics, Part 2: Letters*, vol. 46, no. 29-32, 2007.

[31] G. Brummer, D. Nothern, A. Y. Nikiforov, and T. D. Moustakas, "Deep ultraviolet distributed Bragg reflectors based on graded composition AlGaN alloys," *Applied Physics Letters*, vol. 106, no. 22, 2015.

[32] J. R. Arthur, "Molecular beam epitaxy," *Surface Science*, vol. 500, no. 1-3, pp. 189–217, 2002.

[33] L. Y. L. Shen, "Angular distribution of molecular beams from modified Knudsen cells for molecular-beam epitaxy," *Journal of Vacuum Science and Technology*, vol. 15, no. 1978, p. 10, 1978.

[34] T. Sakamoto, "RHEED oscillations in MBE and their applications to precisely controlled crystal growth," in *Physics, Fabrication, and Applications of Multilayered Structures* (P. Dhez and C. Weisbuch, eds.), pp. 99–109, New York: Plenum Press, 1988.

[35] M. Dabrowska-Szata, "Analysis of RHEED pattern from semiconductor surfaces," *Materials Chemistry and Physics*, vol. 81, no. 2-3, pp. 257–259, 2003.

[36] K. G. Evink, W. T. Taferner, K. Mahalingam, D. L. Dorsey, and S. Adams, "In-situ spectral ellipsometry monitoring/control of mbe growth," in *2000 Digest of the LEOS Summer Topical Meetings. Electronic-Enhanced Optics. Optical Sensing in Semiconductor Manufacturing. Electro-Optics in Space. Broadband Optical Networks (Cat. No.00TH8497)*, pp. II45–II46, July 2000.

[37] V. N. Jmerik, A. M. Mizerov, D. V. Nechaev, P. A. Aseev, A. A. Sitnikova, S. I. Troshkov, P. S. Kop'Ev, and S. V. Ivanov, "Growth of thick AlN epilayers with droplet-free and atomically smooth surface by plasma-assisted molecular beam epitaxy using laser reflectometry monitoring," *Journal of Crystal Growth*, vol. 354, no. 1, pp. 188–192, 2012.

[38] A. Georgakilas, H. M. Ng, and P. Komninou, "Plasma-Assisted Molecular Beam Epitaxy of III V Nitrides," in *Nitride Semiconductors: Handbook on Materials and Devices* (P. Ruterana, M. Albrecht, and J. Neugebauer, eds.), ch. 3, Weinheim: WILEY-VCH Verlag GmbH & Co. KGaA, 2003.

[39] R. G. Banal, M. Funato, and Y. Kawakami, "Growth characteristics of AlN on sapphire substrates by modified migration-enhanced epitaxy," *Journal of Crystal Growth*, vol. 311, no. 10, pp. 2834–2836, 2009.

[40] P. F. Fewster, "X-ray analysis of thin films and multilayers," *Rep. Prog. Phys.*, vol. 59, pp. 1339–1407, 1996.

[41] W. J. Bartels, "Characterization of superlattices by X-ray diffraction," in *Thin Film Growth Techniques for Low-Dimensional Structures* (R. F. C. Farrow, S. S. P. Parkin, P. J. Dobson, J. H. Neave, and A. S. Arrott, eds.), vol. 163, p. 441, New York: Plenum Press, 1987.

[42] G. T. Georgiev and J. J. Butler, "Long-term calibration monitoring of Spectralon diffusers BRDF in the air-ultraviolet," *Applied Optics*, vol. 46, no. 32, p. 7892, 2007.

[43] C.-a. Berseth, A. Scho, O. Dehaese, K. Leifer, A. Rudra, and E. Kapon, "Experimental method for high-accuracy reflectivity-spectrum measurements," *APPLIED OPTICS*, vol. 37, no. 28, pp. 6671–6676, 1998.

[44] S. Mogg, N. Chitica, G. Plaine, and M. Hammar, "Absolute reflectance measurements by a modified cavity phase-shift method Absolute reflectance measurements by a modified cavity phase- shift method," *Review of Scientific Instruments 73,*, vol. 73, no. 1967, 2002.